

Atomically Coupled 2D $\text{MnO}_2/\text{MXene}$ Superlattices for Ultrastable and Fast Aqueous Zinc-Ion Batteries

Yalei Wang, Liwei Liu, Yiping Wang, Junle Qu, Yu Chen,* and Jun Song*



Cite This: *ACS Nano* 2023, 17, 21761–21770



Read Online

ACCESS |

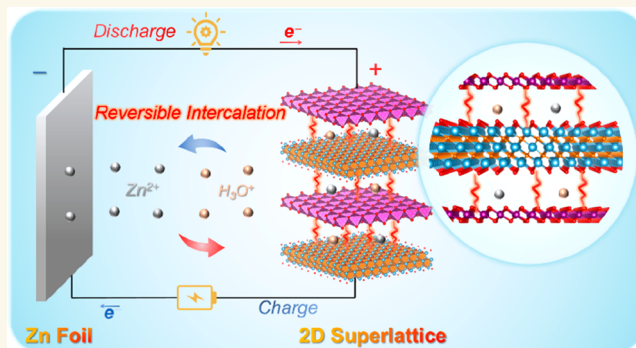
Metrics & More

Article Recommendations

Supporting Information

ABSTRACT: The delta manganese dioxide ($\delta\text{-MnO}_2$) has sparked a great deal of scientific research for application as the cathode in aqueous zinc-ion batteries (AZIBs) owing to its characteristic layered structure. However, further development and commercial application of the $\delta\text{-MnO}_2$ cathode are hindered by the low rate performance and poor cycling stability, which are derived from its inherently poor electrical conductivity and structural instability during the charge/discharge process. Herein, we report the fabrication of the 2D $\text{MnO}_2/\text{MXene}$ superlattice by the solution-phase assembly of unilamellar MnO_2 and $\text{Ti}_3\text{C}_2\text{T}_x$ MXene nanosheets, where the unilamellar MnO_2 nanosheet is separated and stabilized between unilamellar MXene nanosheets. The MXene nanosheets can not only serve as structural stabilizers to isolate the MnO_2 nanosheets and prevent them from aggregating but also act as conductive contributors to strengthen the electrical conductivity, thus maintaining the overall structural stability and realizing the rapid electron transport. Additionally, the regular stacking with a repeating periodicity of the 2D $\text{MnO}_2/\text{MXene}$ can lead to highly exposed active sites, promoting ion diffusion. As a consequence, the large specific capacity of 315.1 mAh g^{-1} at 0.2 A g^{-1} , prominent rate performance of 149.8 mAh g^{-1} at 5 A g^{-1} , and excellent long-term cycling stability after 5000 cycles with 88.1% capacity retention are obtained for the $\text{MnO}_2/\text{MXene}$ cathode in AZIBs. Meanwhile, the superior $\text{H}^+/\text{Zn}^{2+}$ diffusion kinetics and desirable pseudocapacitive behaviors are elucidated by electrochemical measurements and density functional theory computations. This study provides an advanced perspective for the innovation of manganese oxide-based cathode materials in AZIBs.

KEYWORDS: 2D superlattices, MnO_2 nanosheets, MXenes, density functional theory calculations, zinc-ion batteries



INTRODUCTION

Considering the environmental pollution and climatic warming issues related to the combustion of fossil fuels, it is crucial to build a low-carbon society based on green energy sources.^{1,2} However, due to the intermittency nature of green energy sources such as wind, solar, and tidal energy, rechargeable batteries are one of the most effective energy storage media to ensure the continuity of energy supply.^{3,4} In particular, aqueous zinc-ion batteries (AZIBs) have attracted great attention owing to the high theoretical capacity (820 mAh g^{-1}), suitable redox potential (-0.76 V vs standard hydrogen electrode), and low cost of the Zn metal anode as well as the high electrical conductivity, low flammability, and low toxicity of the aqueous electrolyte.^{5–7} As essential components to control the overall performance of batteries, various types of cathode materials, such as manganese-based oxides,^{8,9} vanadium-based oxides,¹⁰ Prussian blue analogues,¹¹ and

organic-based materials,^{12,13} have been widely studied for the storage of Zn^{2+} . Among them, MnO_2 cathodes exhibit high theoretical capacity, large working voltage, and various phases, which have become increasingly important in AZIBs.¹⁴ Particularly, the delta manganese dioxide ($\delta\text{-MnO}_2$) possesses a large interlayer spacing (0.7 nm), which is theoretically more suitable for the rapid and reversible insertion/extraction of Zn^{2+} .¹⁵ Nevertheless, the electrochemical performance of $\delta\text{-MnO}_2$ is far from expectation, which is limited by the

Received: August 14, 2023

Revised: October 24, 2023

Accepted: October 26, 2023

Published: October 27, 2023



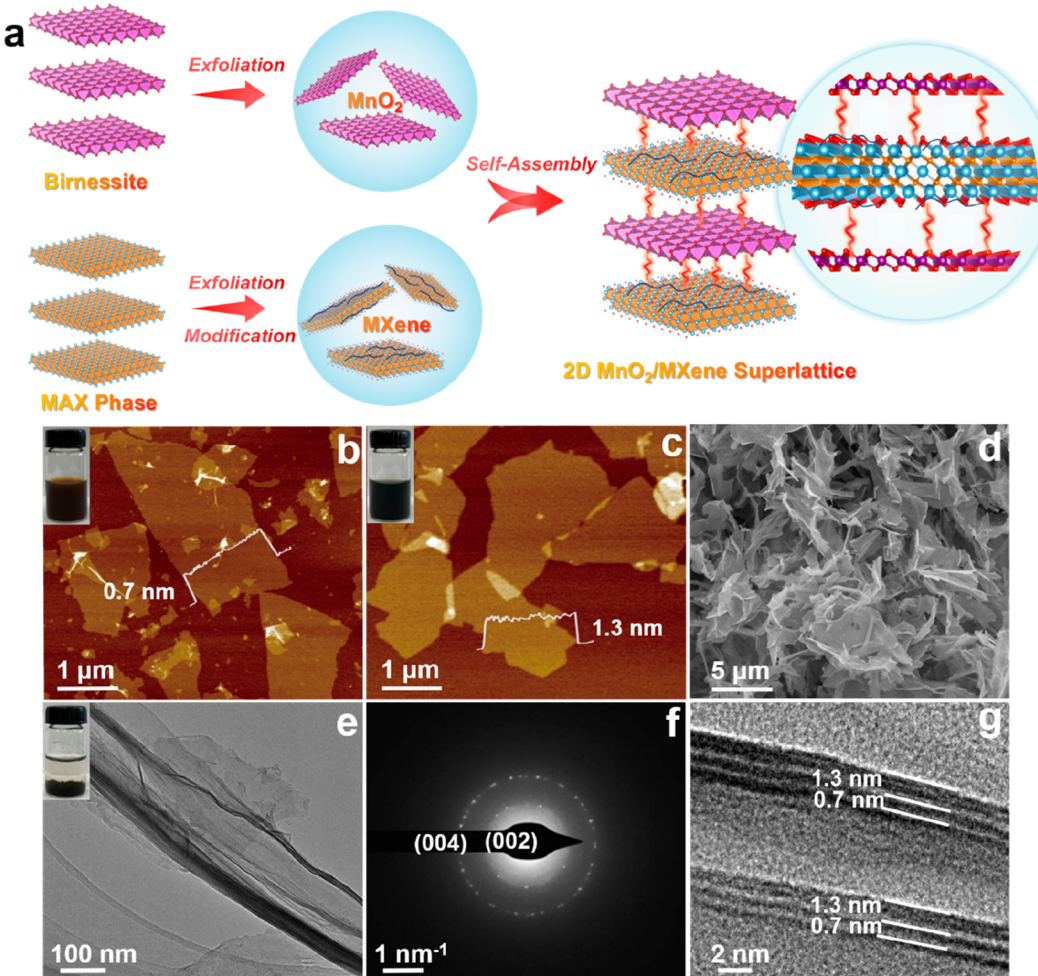


Figure 1. (a) Schematic illustration of the MnO₂/MXene superlattice synthesis. (b, c) AFM images and height profiles for MnO₂ nanosheets (b) and PDDA-MXene nanosheets (c). (d) SEM, (e) TEM, (f) SAED pattern, and (g) HRTEM images of the MnO₂/MXene, respectively.

intrinsically low electrical conductivity and self-aggregation of active materials, giving rise to poor rate performance and cycling stability. To this end, enhancing the electrical conductivity and structural stability of δ-MnO₂ by combining conductive materials is an effective strategy to overcome the above issues.

In general, various carbonaceous materials, such as activated carbon, graphite, carbon nanotubes (CNTs), carbon nanofibers (CNFs), and graphene, have been integrated with δ-MnO₂. However, simply hybridizing them exists in phase separation with a limited degree of synergy, yielding unsatisfactory battery performance. In this context, 2D superlattice structures based on the alternate stacking of two different 2D unilamellar nanosheets, in a well-defined sequence, can readily establish the interconnected ion-electron transport paths and synergistically combine the merits of individual 2D nanosheets while eliminating their limitations (stacking or aggregation).^{16,17} More specifically, 2D superlattices with multiple active sites and large interlayer distances not only show the ability to accommodate large electrolyte ions and reduce the energy barrier of electrolyte ion diffusion but also increase the specific capacity by incorporating a large number of ions into the electrode.¹⁸ In addition, 2D superlattices show the ability to accommodate large mechanical stresses and strains during ion insertion/extraction processes, thereby achieving long cycling life, while 2D

superlattices with excellent electrical conductivity can enable fast electron transport, thereby improving rate performance.¹⁹

MXenes, a rapidly growing family of 2D transition metal carbides, nitrides, and carbonitrides, have shown great potential as electrode materials for electrochemical energy storage devices.^{20,21} Ti₃C₂T_x MXene with metallic conductivity, surface hydrophilicity, and a layered microstructure is the most studied MXene and is produced by selective etching of Al atoms from the Ti₃AlC₂ phases.²² The surface functional groups (−F, −O, and −OH terminal groups) introduced during etching and delamination make Ti₃C₂T_x MXene easily dispersible in aqueous solutions and allow Ti₃C₂T_x MXene to be reassembled with other 2D materials using solution processing techniques.²³ Hence, the metallic conductivity coupled with the superior solution processing capability renders Ti₃C₂T_x MXene an excellent alternative for the carbonaceous material in composite electrodes. Inspired by the above research, combining δ-MnO₂ with Ti₃C₂T_x MXene into 2D superlattice structures may simultaneously enhance the rate performance and cycling stability of δ-MnO₂ electrode materials. Nevertheless, to the best of our knowledge, rational design of the 2D MnO₂/MXene superlattice for AZIBs has not yet been reported.

Herein, we fabricate a 2D MnO₂/MXene superlattice constructed by alternately stacked unilamellar MnO₂ and MXene nanosheets. The regularly layered structure of the 2D

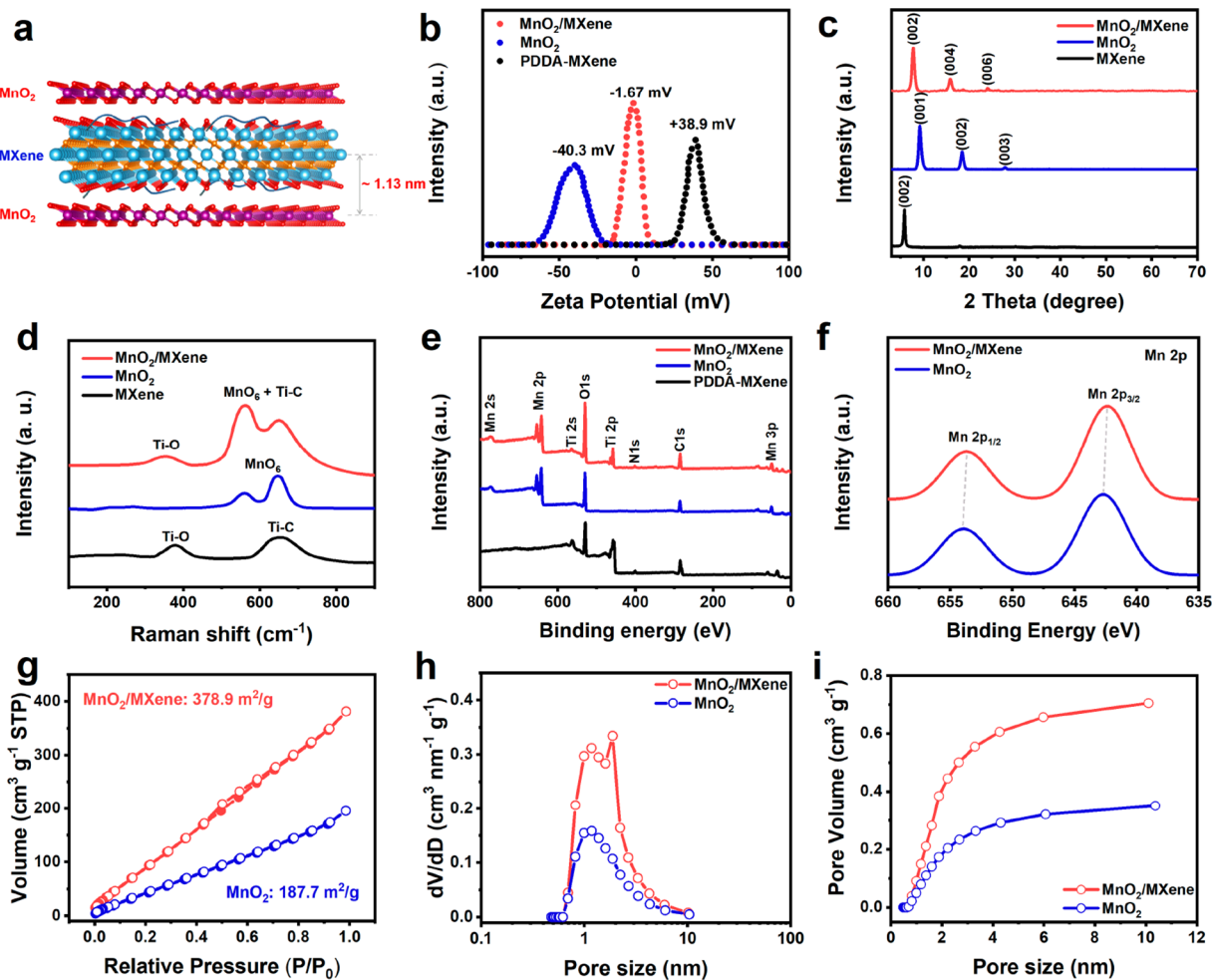


Figure 2. Structure characterizations of the 2D $\text{MnO}_2/\text{MXene}$ superlattice. (a) Crystal structures of the $\text{MnO}_2/\text{MXene}$ superlattice. (b) Zeta potentials of PDDA-MXene, MnO_2 , and $\text{MnO}_2/\text{MXene}$. (c, d) XRD patterns (c) and Raman spectra (d) of MnO_2 , MXene, and $\text{MnO}_2/\text{MXene}$. (e) XPS survey curves of MnO_2 , PDDA-MXene, and $\text{MnO}_2/\text{MXene}$. (f) XPS spectra of Mn 2p. (g) Nitrogen absorption–desorption isotherms. (h, i) The corresponding pore size distribution and pore volume.

$\text{MnO}_2/\text{MXene}$ superlattice endows more active sites, faster electron/ion transports, and fewer structural stresses during the charge/discharge process, which can effectively improve the specific capacity, rate performance, and cycling stability. Thus, the $\text{MnO}_2/\text{MXene}$ cathode exhibits a high capacity of 315.1 mAh g^{-1} at 0.2 A g^{-1} , simultaneously delivering an impressive rate performance of 149.8 mAh g^{-1} at 5 A g^{-1} with excellent long-term cycling stability (88.1% capacity retention after 5000 cycles). In addition, the energy storage mechanism and associated reaction kinetics are systematically investigated by combining experiments and theoretical calculations. Notably, density functional theory (DFT) computations reveal that the regularly layered structure can reduce the diffusion energy barriers between H^+ / Zn^{2+} and host structures, thereby leading to highly reversible H^+ and Zn^{2+} insertion/extraction. This work lays the foundation for the design and development of high-performance layered cathodes in AZIBs.

RESULTS AND DISCUSSION

The 2D $\text{MnO}_2/\text{MXene}$ superlattice was fabricated via a solution-phase assembly of negatively charged MnO_2 and positively charged MXene nanosheets (Figure 1a). The stable suspension of MnO_2 nanosheets is obtained through a typical top-down protonation and chemical delamination approach

(Figures S1 and S2). The scanning electron microscopy (SEM) and transmission electron microscopy (TEM) images clearly present an ultrathin sheetlike morphology (Figure S3). Atomic force microscopy (AFM) images further show a uniform thickness of approximately 0.7 nm, suggesting the formation of unilamellar nanosheets (Figure 1b). The negative surface charge of MnO_2 nanosheets is proved by zeta-potential measurements (Figure 2b). Moreover, the UV–visible (UV–vis) absorption spectrum exhibits a broad absorption peak centered at 374 nm, which is the characteristic of delaminated MnO_2 nanosheets (Figure S7a).²⁴ $\text{Ti}_3\text{C}_2\text{T}_x$ MXene nanosheets are produced by the selective etching of Al layers with tetramethylammonium hydroxide (TMAOH) from the Ti_3AlC_2 MAX phase and subsequent mechanical shaking (Figures S4 and S5). The SEM and TEM images reveal that the as-prepared PDDA-MXene has a flat and nearly transparent sheet-like morphology, indicating its ultrathin thickness (Figure S6). The thickness is uniform and measured as 1.3 nm for the PDDA-MXene nanosheets, in good accordance with the sum value of the crystallographic thickness for a unilamellar MXene nanosheet and cationic media (Figure 1c). In addition, the colloidal suspension of MXene shows an optical absorption band around 262 nm, matching the previously reported MXene nanosheets (Figure S7b).²⁵ The SEM (Figure 1d;

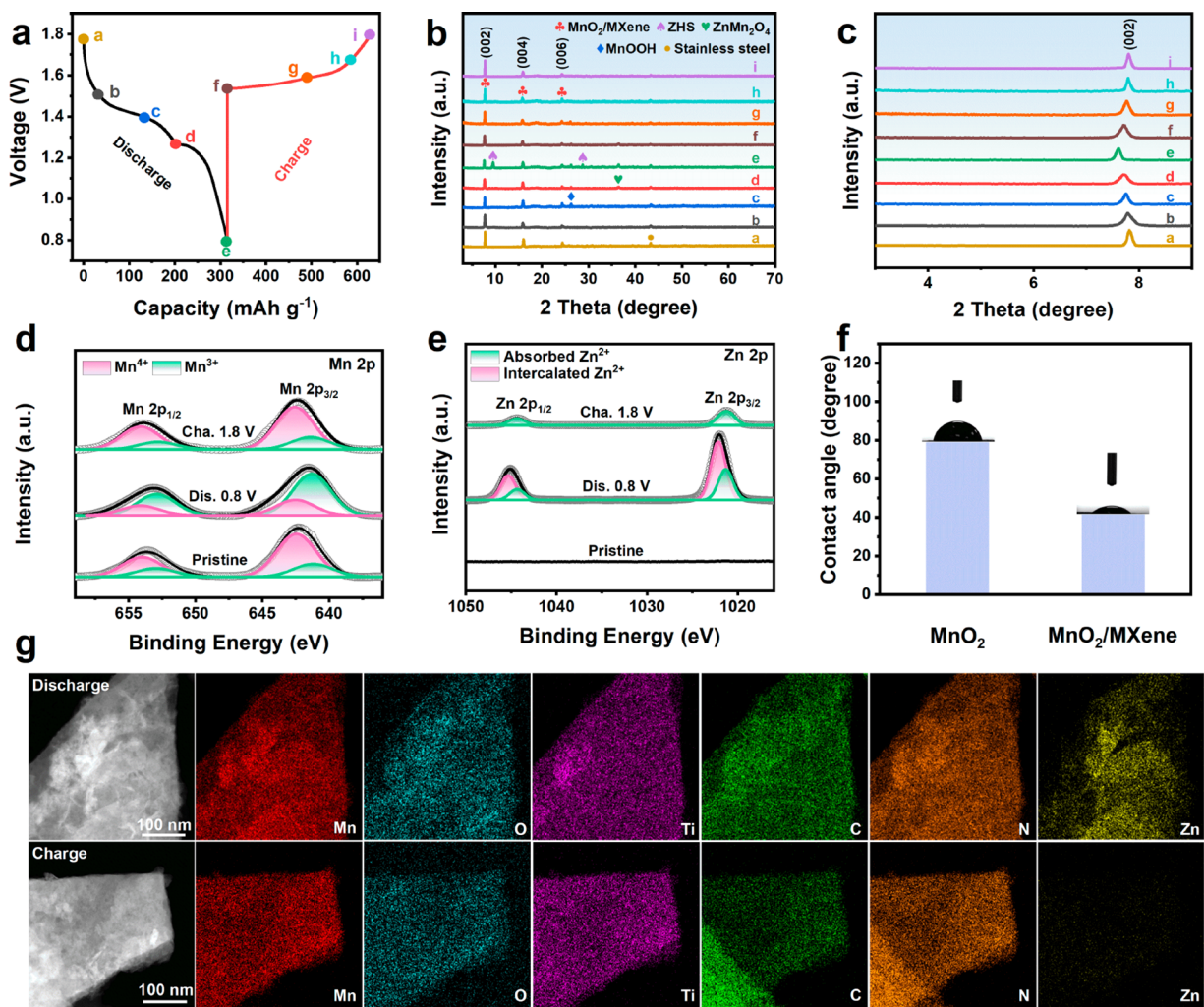


Figure 3. H⁺ and Zn²⁺ storage mechanism studies of the 2D MnO₂/MXene superlattice during the charge/discharge process. (a) Charge/discharge curves under a current density of 0.2 A g⁻¹, in which the marked states are selected for ex situ tests. (b, c) Ex situ XRD patterns. (d, e) Ex situ XPS spectra of Mn 2p (d) and Zn 2p (e). (f) Contact angle of electrolytes on MnO₂ and MnO₂/MXene cathodes. (g) HAADF-STEM and the corresponding elemental mapping images recorded at the fully discharged and charged states.

Figure S8) and TEM images (Figure 1e) of the 2D MnO₂/MXene superlattice exhibit a 3D porous structure composed of wrinkled thin layers, which will facilitate the electrolyte penetration and ion diffusion. The high-angle annular dark-field scanning transmission electron microscope (HAADF-STEM) image and corresponding elemental mapping indicate the uniform distribution of Mn, O, Ti, C, and N elements along the MnO₂/MXene architecture (Figure S9). The selected area electron diffraction (SAED) pattern (Figure 1f) displays the diffraction rings of layered structures based on the MnO₂/MXene superlattice, suggesting regular stacking with repeating periodicity. Furthermore, the high-resolution TEM (HRTEM) image (Figure 1g) reveals parallel lattice fringes with two different spacings in an alternating sequence of 0.7 and 1.3 nm, which corresponds to unilaminar MnO₂ and PDDA-MXene nanosheets, further confirming the formation of the MnO₂/MXene superlattice.

The X-ray diffraction (XRD) patterns of the MnO₂, MXene, and MnO₂/MXene superlattice are shown in Figure 2c. It is obvious that the MnO₂/MXene superlattice forms a regularly layered structure, showing resonance reflections with dominant 00l peaks. The observed d-spacing of 1.13 nm at the low angle is close to half of the combined thickness of the MnO₂ (0.7

nm) and PDDA-MXene (1.3 nm) nanosheets (Figure 2a), which agrees well with the HRTEM result, indicating that the peak should be the second-order reflection of the superlattice structure. These clearly indicate that the MnO₂ and MXene nanosheets are assembled into the 2D superlattice structure with a layer-by-layer pattern. To further illustrate the structure of the 2D MnO₂/MXene superlattice, the Raman spectra are depicted in Figure 2d. The MnO₂ exhibits two strong peaks at 559 and 646 cm⁻¹, which are attributed to the symmetric stretching vibration of the MnO₆ groups.²⁶ For the MXene, two broad peaks are centered at 378 and 652 cm⁻¹, corresponding to the Ti–O and Ti–C vibrations, respectively.²⁷ The 2D MnO₂/MXene superlattice displays the combined characteristics of the two components. It is worth noting that the Ti–O and Ti–C bonds shift to the lower energy positions, which is ascribed to the strong interface interactions between the MnO₂ and MXene nanosheets. The interaction is also confirmed by the Mn 2p X-ray photoelectron spectroscopy (XPS) spectrum collected from the MnO₂/MXene superlattice, where a blue shift of the Mn–O bond is observed compared to the MnO₂ (Figure 2f). In addition, XPS analysis reveals the existence of Mn, O, Ti, C, and N elements in the MnO₂/MXene superlattice (Figure 2e),

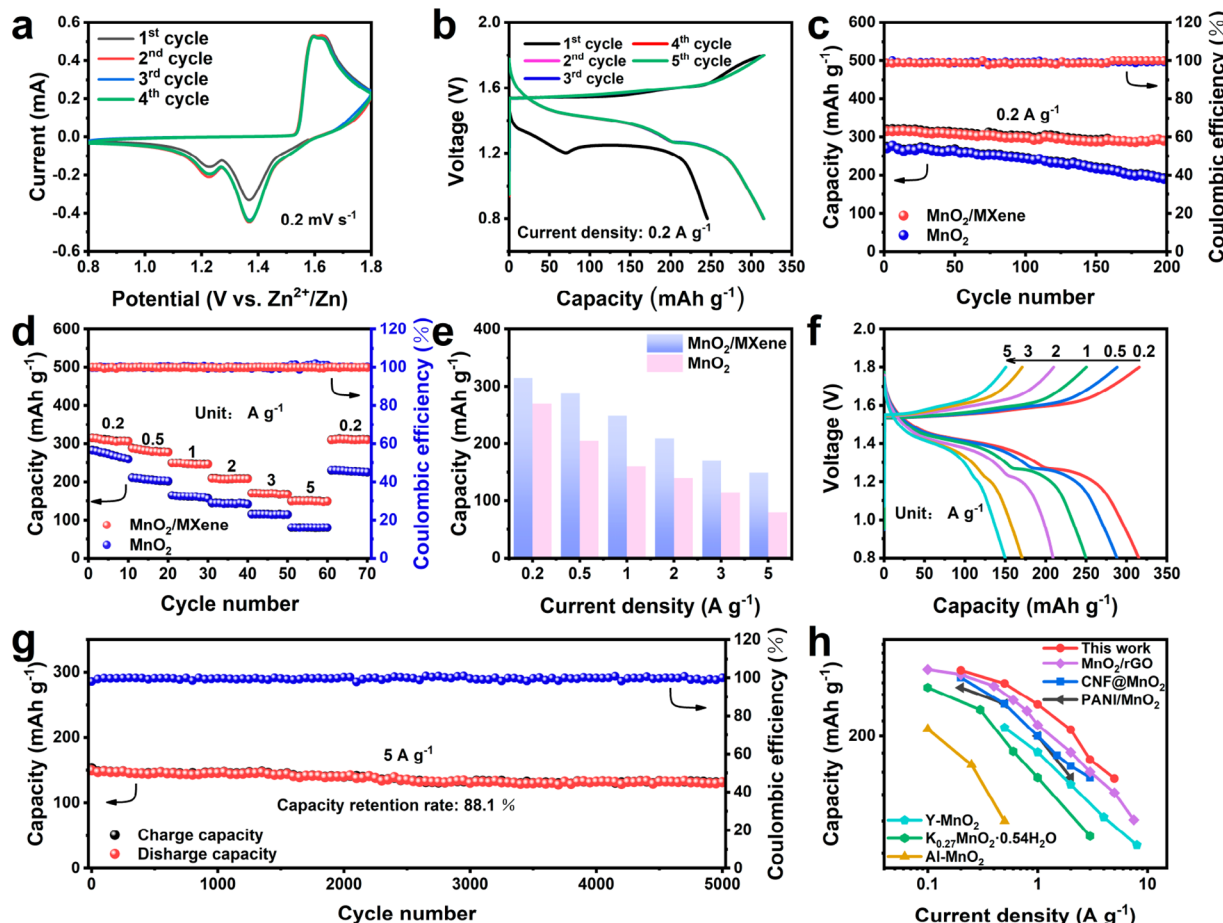


Figure 4. Electrochemical performances of $\text{MnO}_2/\text{MXene}$ cathodes. (a) CV curves at 0.2 mV s^{-1} . (b) Charge–discharge curves at 0.2 A g^{-1} . (c–e) Cycling performances (c), rate performances (d), and average capacities (e) of the MnO_2 and $\text{MnO}_2/\text{MXene}$. (f) Charge/discharge curves at different current densities. (g) Long-term cycling tests at 5 A g^{-1} . (h) Comparison of the rate performance among our $\text{MnO}_2/\text{MXene}$ and reported MnO_2 cathodes for AZIBs.

which is consistent with the elemental mapping results shown in Figure S9. As for the high-resolution O 1s XPS spectrum, there are four fitting peaks located at 529.6, 530.6, 531.7, and 532.9 eV, representing the Mn–O–Mn, Ti–O, Mn–OH, and H–OH bonds, respectively (Figure S11).²⁸ The differences in the exposed surface area of the MnO_2 and $\text{MnO}_2/\text{MXene}$ superlattice are examined by N_2 adsorption–desorption isotherms. As shown in Figure 2g, the $\text{MnO}_2/\text{MXene}$ superlattice shows a Brunauer–Emmett–Teller (BET) surface area of $378.9 \text{ m}^2 \text{ g}^{-1}$ that is higher than that of the MnO_2 ($187.7 \text{ m}^2 \text{ g}^{-1}$). The corresponding pore size distribution of the MnO_2 and $\text{MnO}_2/\text{MXene}$ superlattice from the Barrett–Joyner–Halenda (BJH) analysis demonstrates the coexistence of micropores and mesopores (Figure 2h). Notably, the pore volume of the $\text{MnO}_2/\text{MXene}$ superlattice ($0.76 \text{ cm}^3 \text{ g}^{-1}$) is larger than that of MnO_2 ($0.39 \text{ cm}^3 \text{ g}^{-1}$) (Figure 2i). Consequently, the high surface area and large pore volume of the $\text{MnO}_2/\text{MXene}$ superlattice can provide abundant electroactive sites for the storage of $\text{H}^+/\text{Zn}^{2+}$ ions and increase the contact area between electrode materials and electrolytes, facilitating ion transport and electrolyte penetration.

To explore the energy storage mechanism of the $\text{MnO}_2/\text{MXene}$ cathode during the charge/discharge process, ex situ XRD characterizations were employed to study the electrode structure evolution (Figure 3b,c). The marked states at the second charge/discharge (states a–i) are selected for the ex

situ XRD tests (Figure 3a). As shown in Figure 3b, the (002) peak intensity of the $\text{MnO}_2/\text{MXene}$ cathode is weakening during the discharging process (from states a to e). When the liquid discharges to 1.4 V (state c), a new peak at around 26° emerges, which can be indexed to MnOOH (JPCDS No. 18–0805). This result indicates that the first discharge plateau represents the H^+ insertion process (i.e., $\text{MnO}_2 + \text{H}^+ + \text{e}^- \rightarrow \text{MnOOH}$), which accords well with the previous reports.²⁶ Subsequently, with further discharging to 1.3 V (state d), the diffraction peak of ZnMn_2O_4 (JPCDS No. 24-1133) appears gradually, suggesting that the second discharge plateau corresponds to the Zn^{2+} insertion reaction (i.e., $2\text{MnO}_2 + \text{Zn}^{2+} + 2\text{e}^- \rightarrow \text{ZnMn}_2\text{O}_4$). Then, the typical peaks of zinc sulfate hydroxide hydrate (ZSH, $\text{ZnSO}_4[\text{Zn}(\text{OH})_2]_3 \cdot 3\text{H}_2\text{O}$, JPCDS No. 39-0689) at 9.5° and 28.7° arise in state e. The formation of ZSH is due to the accumulation of OH^- along with the consumption of H^+ (i.e., $4\text{Zn}^{2+} + 6\text{OH}^- + \text{SO}_4^{2-} + 3\text{H}_2\text{O} \rightarrow \text{ZnSO}_4[\text{Zn}(\text{OH})_2]_3 \cdot 3\text{H}_2\text{O}$).²⁹ During the following charging process (from states e to i, the diffraction peaks corresponding to ZHS, ZnMn_2O_4 , and MnOOH gradually disappear. Notably, the pattern is completely restored to the original state after charging back to 1.8 V (state i). Additionally, the characteristic peak (002) shifts to the low angle and gradually recovers to the initial position, and the corresponding interlayer spacing goes from 11.3 to 11.6 Å and progressively recovers back to 11.3 Å (between states a and i).

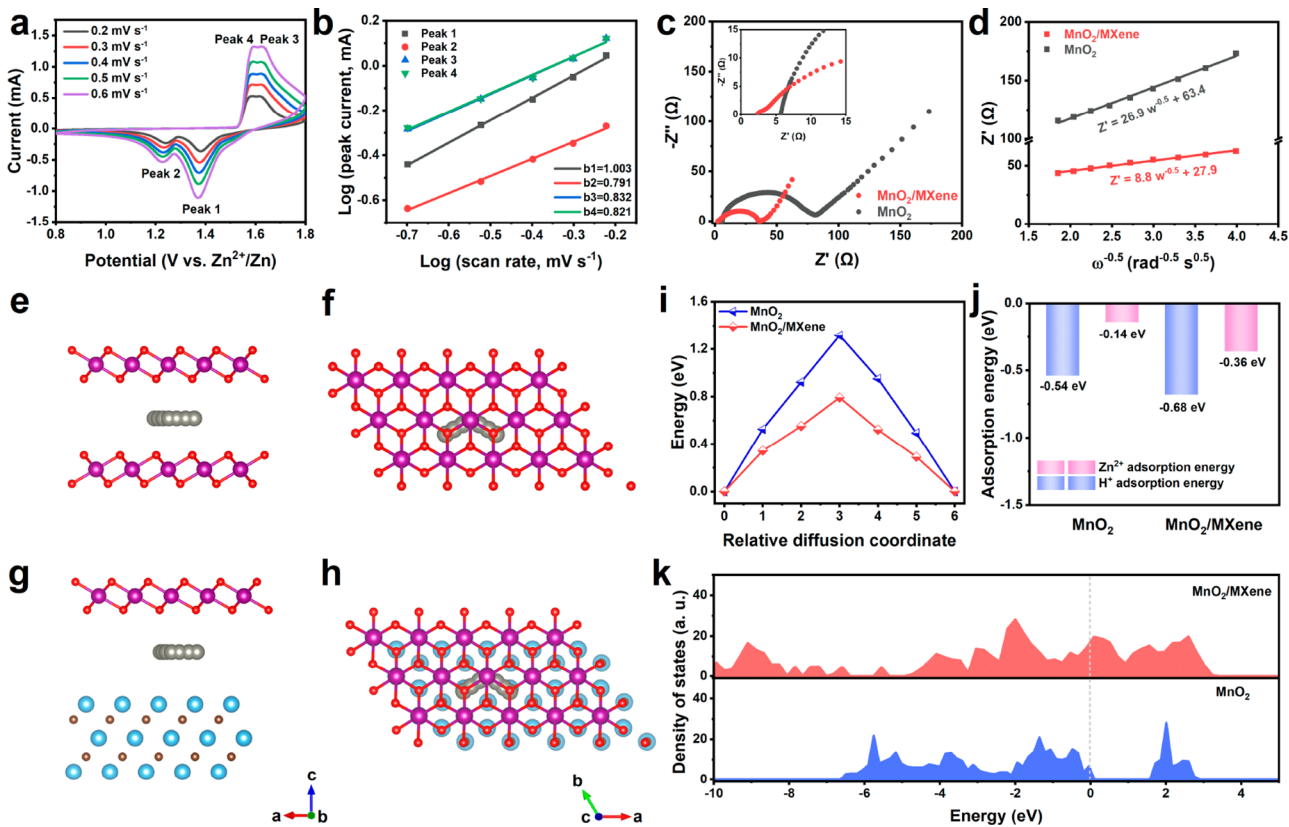


Figure 5. Electrochemical kinetics and DFT calculation results of MnO₂/MXene cathodes. (a) CV curves at various scan rates. (b) log i vs log ν plots according to the CV curves. (c) Nyquist plots of the MnO₂ and MnO₂/MXene. (d) Relationship between the low frequency and real part of the impedance. (e–h) Zn²⁺ diffusion paths in the MnO₂ and MnO₂/MXene from the side view (e, g) and top view (f, h). (i) Corresponding diffusion energy barriers. (j) Absorption energies of H⁺ and Zn²⁺ on the surface of MnO₂ and MnO₂/MXene. (k) DOS for MnO₂ and MnO₂/MXene.

(Figure 3c). In general, ex situ XRD characterizations clearly confirm the reversible insertion/extraction of H⁺ and Zn²⁺ in our MnO₂/MXene cathode during the charge/discharge process.

Moreover, ex situ XPS results of MnO₂/MXene cathodes are presented in Figure 3d,e to further validate the change of valence states during the discharge/charge process. Compared with the initial state, the Mn 2p peaks shift to the low binding energy at the fully discharged state and then return to the high binding energy at the fully charged state, corresponding to the reversible reduction and oxidation of Mn species (Figure 3d). Simultaneously, as observed from the Zn 2p spectra (Figure 3e), there is no Zn signal in the pristine state. After discharging to 0.8 V, two pairs of distinct Zn 2p peaks are detected for the MnO₂/MXene cathode, including intercalated Zn²⁺ and adsorbed Zn²⁺, while there is still a pair of weak Zn 2p peaks after charging to 1.8 V, which is due to the residual surface adsorbed Zn²⁺.³⁰ As expected, this agrees well with the results from HAADF-STEM and the corresponding elemental mapping images (Figure 3g). As a result, the reversible structure evolution and valence change are beneficial to improve the cycling performance of the MnO₂/MXene cathode.

Contact angle measurements were carried out to investigate the surface wettability of the electrodes (Figure 3f). Benefiting from the 2D superlattice structure, the contact angle of the electrolyte on the MnO₂/MXene cathode (41.5°) is significantly reduced relative to the MnO₂ electrode (78.9°),

suggesting that the electrolyte ions more easily to penetrate the MnO₂/MXene cathode surface.³¹ The electrochemical performance of the MnO₂/MXene superlattice was subsequently measured in order to investigate its structural advantages for AZIBs. The areal mass loading of active materials in each electrode is about 1.5 mg cm⁻². Figure 4a shows the cyclic voltammetry (CV) curves of the MnO₂/MXene cathode at 0.2 mV s⁻¹. It is observed that the CV curves are overlapped after the first cycle, indicating a stable and reversible electrochemical process of the MnO₂/MXene cathode. Specifically, two pairs of redox peaks located at 1.37/1.63 and 1.23/1.59 V are attributed to the intercalation/extraction of H⁺ and Zn²⁺, respectively, while two charge/discharge platforms can be detected in the galvanostatic charge/discharge curves (Figure 4b), which are in good agreement with two peak voltages of the oxidation/reduction peaks in CV curves. When tested at a low current density of 0.2 A g⁻¹, the MnO₂/MXene cathode can achieve a specific capacity of 290.8 mAh g⁻¹ after 200 cycles, which is better than that of the MnO₂ cathode (190.6 mAh g⁻¹) (Figure 4c). Correspondingly, there is no obvious change in the morphology after 200 cycles (Figure S13). The improved electrochemical performance of the MnO₂/MXene cathode is further verified by the rate performance and charge/discharge curves at different current densities (Figure 4d–f). As displayed in Figure 4d,f, the MnO₂/MXene cathode can deliver the discharge capacities of 315, 288, 249, 209, 170, and 149 mAh g⁻¹ at 0.2, 0.5, 1.0, 2.0, 3.0, and 5.0 A g⁻¹, respectively. Notably, when the current density goes back to

0.2 A g⁻¹, the discharge capacity is well restored to the initial level. As a comparison, the MnO₂ cathode exhibits an inferior rate performance with only 80.2 mAh g⁻¹ at 5.0 A g⁻¹ (Figure 4e). Moreover, it is worth noting that the MnO₂/MXene cathode shows excellent rate performance compared to previously reported MnO₂-based cathode materials (Figure 4h).^{26,29,32–33,34,35} Additionally, the long-term cycling stability of the MnO₂/MXene cathode was evaluated at a high current density of 5.0 A g⁻¹. From Figure 4g, it can be seen that the MnO₂/MXene cathode manifests a high reversible capacity of 132.1 mAh g⁻¹ after 5000 cycles with a capacity retention of 88.1%. Notably, the MnO₂/MXene cathode shows good morphological stability even after 5000 cycles (Figure S15). In general, the superior rate performance and cycling stability in our rationally designed 2D MnO₂/MXene superlattice should be associated with the following merits: (1) the unilamellar MnO₂ nanosheets are alternately separated by unilamellar MXene nanosheets, enlarging the interlayer spacing and promoting the diffusion of H⁺/Zn²⁺; (2) MXene nanosheets can not only serve as a conductive component for efficient electron transport but also suppress the MnO₂ nanosheet restacking and aggregation to preserve the electrode integrity; (3) the large surface area with abundant micropores and mesopores provides sufficient electrode/electrolyte interfaces, facilitating fast electrolyte ingress and migration; (4) the large pore volume can effectively alleviate the structural stress and buffer the volume change during the H⁺ and Zn²⁺ insertion/extraction. Therefore, 2D MnO₂/MXene superlattices can not only fully highlight the properties of individual 2D components but also realize strong synergistic interactions between them, which is different from the traditional composites that are created by simply mixing different materials without conformal growth and ordered assembly.^{32,33,34,35}

To explore the fundamental reason for the improved electrochemical performance of the MnO₂/MXene cathode, the charge storage behavior and reaction kinetics were investigated by CV, galvanostatic intermittent titration technique (GITT), and electrochemical impedance spectroscopy (EIS) curves. Figure 5a displays the CV curves of the MnO₂/MXene cathode at various scan rates from 0.2 to 0.6 mV s⁻¹. The peak current (i) and scan rate (ν) follow the relation below: $\log i = \log a + b \log \nu$ ($0.5 \leq b \leq 1$), in which a and b are adjustable parameters.³⁶ In general, the slope (b) of 0.5 represents a typical diffusion-controlled process, while the slope (b) of 1.0 demonstrates a characteristic capacitive-controlled process. From the linear fitting curves in Figure 5b, the b values of the four redox peaks for the MnO₂/MXene cathode are calculated as 1.003 (peak 1), 0.791 (peak 2), 0.832 (peak 3), and 0.821 (peak 4), indicating that its charge storage behavior is more inclined to the capacitive-controlled process. To further specify the capacitive contribution at a certain scan rate, according to the equation of $i(V) = k_1\nu + k_2\nu^{1/2}$, where $i(V)$ is the current at a fixed potential (V) and the contributions from diffusion-controlled ($k_2\nu^{1/2}$) and capacitive-controlled ($k_1\nu$) are quantitatively measured.³⁷ For example, at a scan rate of 0.6 mV s⁻¹, the blue region in the entire CV curve represents the capacitive-controlled capacity, which accounts for 81.5% of the total capacity (Figure S16). Obviously, the capacitive contribution of the MnO₂/MXene cathode gradually grows from 69.1% at 0.2 mV s⁻¹ to 81.5% at 0.6 mV s⁻¹ (Figure S17), which is greater than that of the MnO₂ cathode (Figure S18). In addition, the Nyquist plots of

MnO₂ and MnO₂/MXene cathodes measured by EIS are shown in Figure 5c. It is obvious that the two Nyquist curves are composed of near semicircles in the high-frequency region and oblique straight lines in the low-frequency region. The MnO₂/MXene cathode present a lower ohmic resistance (2.37 Ω) than that of the MnO₂ cathode (5.71 Ω). The semicircle of the MnO₂/MXene cathode, which is related to the charge transfer resistance, is much smaller than that of the MnO₂ cathode, confirming that MXene is beneficial to increasing the conductivity of the MnO₂/MXene cathode. Meanwhile, the slope of the Warburg line increases, indicating improved diffusion of ions to the electrode. Specifically, the ion diffusion coefficient (D_{ion}) can be obtained quantitatively based on the relationship between the low frequency and real part of impedance (details shown in the Supporting Information).³⁸ As shown in Figure 5d, the D_{ion} of the MnO₂/MXene cathode is calculated to be 1.43×10^{-9} cm² s⁻¹, which is higher than that of the MnO₂ cathode (1.53×10^{-10} cm² s⁻¹), revealing that the 2D superlattice structure of the MnO₂/MXene enables faster diffusion of H⁺ and Zn²⁺. GITT measurement was also performed to estimate the D_{ion} value (Figures S19 and S20, details described in the Supporting Information). As calculated, the D_{ion} values of the MnO₂/MXene cathode mainly stay in the magnitude range from 10^{-9} to 10^{-8} cm² s⁻¹ during the charge–discharge process, ensuring the high rate performance, which is consistent with the EIS results.

To further delve into the excellent electrochemical performance of MnO₂/MXene cathodes, DFT calculations were performed to analyze the intrinsic influence of 2D superlattice structures on the H⁺ and Zn²⁺ dynamics process. Figure 5k shows the density of states (DOS) of MnO₂ and MnO₂/MXene. In contrast, the DOS of the MnO₂/MXene greatly increases near the Fermi level, indicating that the introduction of 2D superlattice structures dramatically changes the DOS of the MnO₂ and thus significantly improves its electrical conductivity.³⁹ Moreover, the differential charge density analysis depicted in Figure S21 displays the interfacial electron interactions and distributions of MnO₂ and MnO₂/MXene. Obviously, MnO₂/MXene has more electron transfer than MnO₂ (Table S1), which also proves that the 2D superlattice structure helps to improve the electrical conductivity. In addition, the adsorption energies of the H⁺ and Zn²⁺ on the MnO₂/MXene surface are -0.68 and -0.36 eV, respectively, while the adsorption energies of the H⁺ and Zn²⁺ on the MnO₂ surface are -0.54 and -0.14 eV, respectively (Figure 5j). The more negative adsorption energy reveals that H⁺ and Zn²⁺ are more easily adsorbed on the MnO₂/MXene surface, so the ion transfer between the electrode surface and the electrolyte is more likely to occur.⁴⁰ To further investigate the diffusion of H⁺ and Zn²⁺ between the interlayer of MnO₂ and MnO₂/MXene, the diffusion paths are shown in Figure 5e–h and Figure S22a,b. Notably, the ion diffusion energy barriers in the MnO₂/MXene are much lower than that in the MnO₂ (Figure 5i; Figure S22c), confirming the ultrafast H⁺ and Zn²⁺ transport capability of the MnO₂/MXene. Therefore, the improved electrical conductivity, more negative adsorption energy, and lower diffusion energy barriers enable superior rate performance.

CONCLUSIONS

In summary, benefiting from the synergism of alternately stacked unilamellar MnO₂ and MXene nanosheets in accelerating ion/electron transfer dynamics and enhancing

structural stabilities, the 2D $\text{MnO}_2/\text{MXene}$ cathode exhibits extraordinary electrochemical performance in AZIBs. Briefly, it delivers a high capacity of 290.8 mAh g^{-1} after 200 cycles at 0.2 A g^{-1} . Even at a high current density of 5 A g^{-1} , a considerable reversible capacity of 132.1 mAh g^{-1} can still be maintained after 5000 cycles, with a capacity retention of 88.1%. Additionally, the structural stability and reversible $\text{H}^+/\text{Zn}^{2+}$ insertion/extraction of 2D $\text{MnO}_2/\text{MXene}$ superlattices were investigated by *ex situ* XRD, XPS, and TEM. Moreover, the energy storage mechanism and associated reaction kinetics involving pseudocapacitive behaviors, ion diffusion coefficients, and diffusion energy barriers were fully researched and discussed through CV, EIS, and GITT measurements and DFT computations.

METHODS

Preparation of the MnO_2 Nanosheets. K-birnessite nanobelts (K-MnO_2) were synthesized by a hydrothermal method. In a typical procedure, $\text{MnCl}_2 \cdot 4\text{H}_2\text{O}$ was added into 8 mL of deionized water (called solution A), and then KMnO_4 (3 mmol) and KOH (1.8 mmol) were dissolved into 84 mL of deionized water under vigorous stirring to obtain a dark green solution (called solution B). Then, solution A was quickly added into solution B to form a dark brown solution, after which the mixture was allowed to cool slowly with continuous stirring for 2 h. The resulting mixture was transferred to a Teflon-lined stainless steel autoclave and maintained at 175°C for 48 h. Subsequently, the resulting precipitate was filtered, washed several times with deionized water, and then air-dried. To obtain H-birnessite (H-MnO_2) nanobelts, K-MnO_2 (1 g) was successively treated with 250 mL of 0.5 M $(\text{NH}_4)_2\text{S}_2\text{O}_8$ at 60°C for 12 h and 1 M HCl at 25°C for 2 h. The solid was collected by filtration, washed several times with deionized water, and then dried in the air. Finally, 0.2 g of as-prepared H- MnO_2 was immersed in 50 mL of 25 wt % tetramethylammonium hydroxide (TMAOH) aqueous solution and stirred for 48 h. After this, the as-obtained mixture was repeatedly centrifuged with deionized water until the supernatant solution became neutral. The centrifuged pastelike sediment was redispersed in deionized water and shaken at 120 rpm for 48 h. The MnO_2 nanosheet suspension was collected by centrifugation at 3500 rpm for 15 min to remove the unexfoliated portion.

Preparation of the $\text{Ti}_3\text{C}_2\text{T}_x$ MXene Nanosheets. Ti_3AlC_2 MAX crystals (1 g) were treated with 10 wt % hydrofluoric acid (HF) and stirred for 15 min to remove the oxide passivation layer on the surface. After the HF treatment, the powder was washed several times by centrifuging with deionized water until the supernatant solution became neutral. Then, the precipitate was dispersed in a mixed solution of 25 wt % TMAOH (5 mL) and deionized water (5 mL) for 24 h under stirring to etch the interlayer Al layers, obtaining multilayer $\text{Ti}_3\text{C}_2\text{T}_x$ with an accordion-like structure. The resulting dispersion was washed with deionized water for a few times until the pH reached near neutral and the sediment was redispersed in deionized water and shaken for 12 h. Finally, $\text{Ti}_3\text{C}_2\text{T}_x$ MXene nanosheets were obtained after centrifugation at 3500 rpm for 30 min.

Preparation of the $\text{MnO}_2/\text{MXene}$ Superlattices. 100 mL of $\text{Ti}_3\text{C}_2\text{T}_x$ MXene suspension (1 mg mL^{-1}) was mixed with 10 mL of poly(diallyldimethylammonium chloride) (PDDA) solution (10 wt %), and the mixture was stirred for 60 h. The resulting slurry was centrifuged at a high speed of 10000 rpm, and then the precipitate was washed several times and redispersed in deionized water after ultrasonic treatment. Subsequently, a stable PDDA-MXene suspension with a positively charged nature was obtained by collecting the supernatant after centrifugation at 4000 rpm (Figure S10; Figure 2b). To obtain the $\text{MnO}_2/\text{MXene}$ superlattice, suspensions of PDDA-MXene and MnO_2 nanosheets were mixed dropwise at a mass ratio of 3:7 with continuous stirring. Upon mixing the suspensions of MnO_2 and PDDA-MXene nanosheets, a distinct flocculation phenomenon is observed due to electrostatic attraction, implying the successful formation of the 2D $\text{MnO}_2/\text{MXene}$ superlattice (Figure 1e). The

flocculated $\text{MnO}_2/\text{MXene}$ was collected by centrifugation and then freeze-dried.

ASSOCIATED CONTENT

Supporting Information

The Supporting Information is available free of charge at <https://pubs.acs.org/doi/10.1021/acsnano.3c07627>.

Additional experimental details including characterizations, electrochemical measurements, details of first-principle calculations and calculations of the ion diffusion coefficient; SEM images and XRD patterns of the H- MnO_2 and K- MnO_2 precursors; SEM images and XRD patterns of the MAX and multilayer MXene; SEM and TEM images of the MnO_2 and PDDA-MXene nanosheets; UV-vis absorption spectra of the MnO_2 and MXene solution; SEM and the corresponding elemental mapping images of the $\text{MnO}_2/\text{MXene}$ superlattice; HAADF-STEM and the corresponding elemental mapping images of the $\text{MnO}_2/\text{MXene}$ superlattice; Zeta potential of the MXene solution; XPS spectra; charge/discharge curves of MXene nanosheets; HRTEM images of the $\text{MnO}_2/\text{MXene}$ after 200 cycles; cycling tests of MnO_2 ; SEM images of $\text{MnO}_2/\text{MXene}$ cathodes before and after 5000 cycles; CV curves of the MnO_2 at various scan rates and $\text{MnO}_2/\text{MXene}$ cathodes with a capacitive contribution ratio at 0.6 mV s^{-1} ; capacitive and diffusion-controlled contribution ratios; GITT curves and the corresponding ion diffusion coefficients; differential charge densities with the H^+ and Zn^{2+} intercalation in the MnO_2 and $\text{MnO}_2/\text{MXene}$; H^+ diffusion paths in the MnO_2 and $\text{MnO}_2/\text{MXene}$ from the side view; diffusion energy barriers; table showing charge transfer of H^+ and Zn^{2+} inserted into MnO_2 and $\text{MnO}_2/\text{MXene}$ (PDF)

AUTHOR INFORMATION

Corresponding Authors

Yu Chen – State Key Laboratory of Radio Frequency Heterogeneous Integration (Shenzhen University); College of Physics and Optoelectronic Engineering, Key Laboratory of Optoelectronic Devices and Systems of Ministry of Education and Guangdong Province, Shenzhen University, Shenzhen 518060, P.R. China; Email: chenyu2016@szu.edu.cn

Jun Song – State Key Laboratory of Radio Frequency Heterogeneous Integration (Shenzhen University); College of Physics and Optoelectronic Engineering, Key Laboratory of Optoelectronic Devices and Systems of Ministry of Education and Guangdong Province, Shenzhen University, Shenzhen 518060, P.R. China; orcid.org/0000-0002-2321-7064; Email: songjun@szu.edu.cn

Authors

Yalei Wang – State Key Laboratory of Radio Frequency Heterogeneous Integration (Shenzhen University); College of Physics and Optoelectronic Engineering, Key Laboratory of Optoelectronic Devices and Systems of Ministry of Education and Guangdong Province, Shenzhen University, Shenzhen 518060, P.R. China

Liwei Liu – State Key Laboratory of Radio Frequency Heterogeneous Integration (Shenzhen University); College of Physics and Optoelectronic Engineering, Key Laboratory of Optoelectronic Devices and Systems of Ministry of Education

and Guangdong Province, Shenzhen University, Shenzhen 518060, P.R. China; orcid.org/0000-0002-4593-665X

Yiping Wang – State Key Laboratory of Radio Frequency Heterogeneous Integration (Shenzhen University); College of Physics and Optoelectronic Engineering, Key Laboratory of Optoelectronic Devices and Systems of Ministry of Education and Guangdong Province, Shenzhen University, Shenzhen 518060, P.R. China

Junle Qu – State Key Laboratory of Radio Frequency Heterogeneous Integration (Shenzhen University); College of Physics and Optoelectronic Engineering, Key Laboratory of Optoelectronic Devices and Systems of Ministry of Education and Guangdong Province, Shenzhen University, Shenzhen 518060, P.R. China

Complete contact information is available at:
<https://pubs.acs.org/10.1021/acsnano.3c07627>

Notes

The authors declare no competing financial interest.

ACKNOWLEDGMENTS

This work was supported by the National Natural Science Foundation of China (52102268/62175161/61835009/62127819), China Postdoctoral Science Foundation (2023T160432), National Key R&D Program of China (2021YFF0502900), Shenzhen Science and Technology Program (JCYJ20210324095810028), and Shenzhen Key Laboratory of Photonics and Biophotonics (ZDSYS20210623092006020). We thank the Instrument Analysis Center of Shenzhen University for the assistance with TEM analysis.

REFERENCES

- (1) Liang, Y.; Yao, Y. Designing modern aqueous batteries. *Nat. Rev. Mater.* **2023**, *8* (2), 109–122.
- (2) Wang, C.; Wang, D.; Lv, D.; Peng, H.; Song, X.; Yang, J.; Qian, Y. Interface Engineering by Hydrophilic and Zincophilic Aluminum Hydroxide Fluoride for Anode-Free Zinc Metal Batteries at Low Temperature. *Adv. Energy Mater.* **2023**, *13*, 2204388.
- (3) Huang, S.; Hou, L.; Li, T.; Jiao, Y.; Wu, P. Antifreezing Hydrogel Electrolyte with Ternary Hydrogen Bonding for High-Performance Zinc-Ion Batteries. *Adv. Mater.* **2022**, *34* (14), 2110140.
- (4) Li, J.; Luo, N.; Kang, L.; Zhao, F.; Jiao, Y.; Macdonald, T. J.; Wang, M.; Parkin, I. P.; Shearing, P. R.; Brett, D. J. L.; et al. Hydrogen-Bond Reinforced Superstructural Manganese Oxide As the Cathode for Ultra-Stable Aqueous Zinc Ion Batteries. *Adv. Energy Mater.* **2022**, *12* (44), 202201840.
- (5) Zhang, J.; Li, W.; Wang, J.; Pu, X.; Zhang, G.; Wang, S.; Wang, N.; Li, X. Engineering p-Band Center of Oxygen Boosting H⁺ Intercalation in δ-MnO₂ for Aqueous Zinc Ion Batteries. *Angew. Chem., Int. Ed.* **2023**, *62* (8), No. e202215654.
- (6) Cao, Z.; Zhuang, P.; Zhang, X.; Ye, M.; Shen, J.; Ajayan, P. M. Strategies for Dendrite-Free Anode in Aqueous Rechargeable Zinc Ion Batteries. *Adv. Energy Mater.* **2020**, *10* (30), 202001599.
- (7) Wang, D.; Li, Q.; Zhao, Y.; Hong, H.; Li, H.; Huang, Z.; Liang, G.; Yang, Q.; Zhi, C. Insight on Organic Molecules in Aqueous Zn-Ion Batteries with an Emphasis on the Zn Anode Regulation. *Adv. Energy Mater.* **2022**, *12* (9), 202102707.
- (8) Li, M.; He, Q.; Li, Z.; Li, Q.; Zhang, Y.; Meng, J.; Liu, X.; Li, S.; Wu, B.; Chen, L.; et al. A novel dendrite-free Mn²⁺/Zn²⁺ hybrid battery with 2.3 V voltage window and 11000-cycle lifespan. *Adv. Energy Mater.* **2019**, *9* (29), 201901469.
- (9) Chao, D.; Zhou, W.; Ye, C.; Zhang, Q.; Chen, Y.; Gu, L.; Davey, K.; Qiao, S. Z. An Electrolytic Zn-MnO₂ Battery for High-Voltage and Scalable Energy Storage. *Angew. Chem., Int. Ed.* **2019**, *131* (23), 7905–7910.
- (10) Ding, J.; Du, Z.; Li, B.; Wang, L.; Wang, S.; Gong, Y.; Yang, S. Unlocking the Potential of Disordered Rocksalts for Aqueous Zinc-Ion Batteries. *Adv. Mater.* **2019**, *31* (44), 1904369.
- (11) Yang, Q.; Mo, F.; Liu, Z.; Ma, L.; Li, X.; Fang, D.; Chen, S.; Zhang, S.; Zhi, C. Activating C-Coordinated Iron of Iron Hexacyanoferrate for Zn Hybrid-Ion Batteries with 10000-Cycle Lifespan and Superior Rate Capability. *Adv. Mater.* **2019**, *31* (32), 1901521.
- (12) Guo, Z.; Ma, Y.; Dong, X.; Huang, J.; Wang, Y.; Xia, Y. An Environmentally Friendly and Flexible Aqueous Zinc Battery Using an Organic Cathode. *Angew. Chem., Int. Ed.* **2018**, *57* (36), 11737–11741.
- (13) Wang, N.; Dong, X.; Wang, B.; Guo, Z.; Wang, Z.; Wang, R.; Qiu, X.; Wang, Y. Zinc–organic battery with a wide operation-temperature window from –70 to 150°C. *Angew. Chem., Int. Ed.* **2020**, *59* (34), 14577–14583.
- (14) Zhu, X.; Cao, Z.; Wang, W.; Li, H.; Dong, J.; Gao, S.; Xu, D.; Li, L.; Shen, J.; Ye, M. Superior-Performance Aqueous Zinc-Ion Batteries Based on the In Situ Growth of MnO₂ Nanosheets on V₂CT_X MXene. *ACS Nano* **2021**, *15* (2), 2971–2983.
- (15) Xiong, T.; Zhang, Y.; Lee, W. S. V.; Xue, J. Defect Engineering in Manganese-Based Oxides for Aqueous Rechargeable Zinc-Ion Batteries: A Review. *Adv. Energy Mater.* **2020**, *10* (34), 2001769.
- (16) Wang, S.; Zhao, S.; Guo, X.; Wang, G. 2D Material-Based Heterostructures for Rechargeable Batteries. *Adv. Energy Mater.* **2022**, *12* (4), 2100864.
- (17) Xiong, P.; Sun, B.; Sakai, N.; Ma, R.; Sasaki, T.; Wang, S.; Zhang, J.; Wang, G. 2D Superlattices for Efficient Energy Storage and Conversion. *Adv. Mater.* **2020**, *32* (18), 1902654.
- (18) Xiong, P.; Ma, R.; Sakai, N.; Nurdwijayanto, L.; Sasaki, T. Unilamellar Metallic MoS₂/Graphene Superlattice for Efficient Sodium Storage and Hydrogen Evolution. *ACS Energy Lett.* **2018**, *3* (4), 997–1005.
- (19) Xiong, P.; Zhang, X.; Zhang, F.; Yi, D.; Zhang, J.; Sun, B.; Tian, H.; Shanmukaraj, D.; Rojo, T.; Armand, M.; et al. Two-Dimensional Unilamellar Cation-Deficient Metal Oxide Nanosheet Superlattices for High-Rate Sodium Ion Energy Storage. *ACS Nano* **2018**, *12* (12), 12337–12346.
- (20) Ghidiu, M.; Lukatskaya, M. R.; Zhao, M. Q.; Gogotsi, Y.; Barsoum, M. W. Conductive two-dimensional titanium carbide ‘clay’ with high volumetric capacitance. *Nature* **2014**, *516* (7529), 78–81.
- (21) Anasori, B.; Lukatskaya, M. R.; Gogotsi, Y. 2D metal carbides and nitrides (MXenes) for energy storage. *Nat. Rev. Mater.* **2017**, *2* (2), 1–17.
- (22) Zhang, Y.; Yuan, Z.; Zhao, L.; Li, Y.; Qin, X.; Li, J.; Han, W.; Wang, L. Review of Design Routines of MXene Materials for Magnesium-Ion Energy Storage Device. *Small* **2023**, *19*, 2301815.
- (23) Akuzum, B.; Maleski, K.; Anasori, B.; Lelyukh, P.; Alvarez, N. J.; Kumbur, E. C.; Gogotsi, Y. Rheological Characteristics of 2D Titanium Carbide (MXene) Dispersions: A Guide for Processing MXenes. *ACS Nano* **2018**, *12* (3), 2685–2694.
- (24) Omomo, Y.; Sasaki, T.; Wang, L.; Watanabe, M. Redoxable nanosheet crystallites of MnO₂ derived via delamination of a layered manganese oxide. *J. Am. Chem. Soc.* **2003**, *125* (12), 3568–3575.
- (25) Wang, Z.; Xuan, J.; Zhao, Z.; Li, Q.; Geng, F. Versatile Cutting Method for Producing Fluorescent Ultrasmall MXene Sheets. *ACS Nano* **2017**, *11* (11), 11559–11565.
- (26) Wang, J.; Wang, J. G.; Liu, H.; You, Z.; Li, Z.; Kang, F.; Wei, B. A Highly Flexible and Lightweight MnO₂/Graphene Membrane for Superior Zinc-Ion Batteries. *Adv. Funct. Mater.* **2021**, *31* (7), 2007397.
- (27) Naguib, M.; Kurtoglu, M.; Presser, V.; Lu, J.; Niu, J.; Heon, M.; Hultman, L.; Gogotsi, Y.; Barsoum, M. W. Two-dimensional nanocrystals produced by exfoliation of Ti₃AlC₂. *Adv. Mater.* **2011**, *23* (37), 4248–4253.
- (28) Yang, Q.; Qu, X.; Cui, H.; He, X.; Shao, Y.; Zhang, Y.; Guo, X.; Chen, A.; Chen, Z.; Zhang, R.; et al. Rechargeable Aqueous Mn-Metal

Battery Enabled by Inorganic–Organic Interfaces. *Angew. Chem., Int. Ed.* **2022**, *61* (35), No. e202206471.

(29) Liu, L.; Wu, Y. C.; Huang, L.; Liu, K.; Dupoyer, B.; Rozier, P.; Taberna, P. L.; Simon, P. Alkali Ions Pre-Intercalated Layered MnO₂ Nanosheet for Zinc-Ions Storage. *Adv. Energy Mater.* **2021**, *11* (31), 2101287.

(30) Chen, S.; Li, K.; Hui, K. S.; Zhang, J. Regulation of Lamellar Structure of Vanadium Oxide via Polyaniline Intercalation for High-Performance Aqueous Zinc-Ion Battery. *Adv. Funct. Mater.* **2020**, *30* (43), 2003890.

(31) Wang, W.; Huang, G.; Wang, Y.; Cao, Z.; Cavallo, L.; Hedhili, M. N.; Alshareef, H. N. Organic Acid Etching Strategy for Dendrite Suppression in Aqueous Zinc-Ion Batteries. *Adv. Energy Mater.* **2022**, *12* (6), 2102797.

(32) Huang, J.; Wang, Z.; Hou, M.; Dong, X.; Liu, Y.; Wang, Y.; Xia, Y. Polyaniline-intercalated manganese dioxide nanolayers as a high-performance cathode material for an aqueous zinc-ion battery. *Nat. Commun.* **2018**, *9* (1), 2906.

(33) Wu, T. H.; Lin, Y. Q.; Huang, J. X. Yttrium-preintercalated layered manganese oxide as a durable cathode for aqueous zinc-ion batteries. *Nanoscale* **2023**, *15* (4), 1869–1879.

(34) Chomkhundot, P.; Hantanasirisakul, K.; Duangdangchote, S.; Phattharasupakun, N.; Sawangphruk, M. The charge density of intercalants inside layered birnessite manganese oxide nanosheets determining Zn-ion storage capability towards rechargeable Zn-ion batteries. *J. Mater. Chem. A* **2022**, *10* (10), 5561–5568.

(35) Chen, X.; Li, W.; Zeng, Z.; Reed, D.; Li, X.; Liu, X. Engineering stable Zn-MnO₂ batteries by synergistic stabilization between the carbon nanofiber core and birnessite-MnO₂ nanosheets shell. *Chemical Engineering Journal* **2021**, *405*, 126969.

(36) Wang, X.; Li, Y.; Wang, S.; Zhou, F.; Das, P.; Sun, C.; Zheng, S.; Wu, Z. S. 2D Amorphous V₂O₅/Graphene Heterostructures for High-Safety Aqueous Zn-Ion Batteries with Unprecedented Capacity and Ultrahigh Rate Capability. *Adv. Energy Mater.* **2020**, *10* (22), 202000081.

(37) Yuan, Z.; Lin, Q.; Li, Y.; Han, W.; Wang, L. Effects of Multiple Ion Reactions Based on a CoSe₂/MXene Cathode in Aluminum-Ion Batteries. *Adv. Mater.* **2023**, *35* (17), 2211527.

(38) Cai, P.; Momen, R.; Tian, Y.; Yang, L.; Zou, K.; Massoudi, A.; Deng, W.; Hou, H.; Zou, G.; Ji, X. Advanced Pre-Diagnosis Method of Biomass Intermediates Toward High Energy Dual-Carbon Potassium-Ion Capacitor. *Adv. Energy Mater.* **2022**, *12* (5), 2103221.

(39) Wu, L.; Sun, L.; Li, X.; Zhang, Q.; Zhang, Y.; Gu, J.; Wang, K.; Zhang, Y. CuCo₂S₄–rGO Microflowers: First-Principle Calculation and Application in Energy Storage. *Small* **2020**, *16* (28), 2001468.

(40) Yan, M.; He, P.; Chen, Y.; Wang, S.; Wei, Q.; Zhao, K.; Xu, X.; An, Q.; Shuang, Y.; Shao, Y.; et al. Water-lubricated intercalation in V₂O₅·nH₂O for high-capacity and high-rate aqueous rechargeable zinc batteries. *Adv. Mater.* **2018**, *30* (1), 1703725.

□ Recommended by ACS

Nanostructure Design of MnO₂/Partially Oxidized Graphene Nanocomposite Cathode via One-Step Pulse Potential Strategy: Toward Ultralong-Life Zinc-Ion Batteries

Shabnam Saadi-motaallegh, Biao Gao, *et al.*

NOVEMBER 10, 2023

ACS APPLIED ENGINEERING MATERIALS

READ ↗

High Electrochemical Capacity MnO₂/Graphene Hybrid Fibers Based on Crystalline Regulatable MnO₂ for Wearable Supercapacitors

Xiaojuan Tian, Qufu Wei, *et al.*

OCTOBER 31, 2023

ACS APPLIED MATERIALS & INTERFACES

READ ↗

Layered Topological Insulator MnBi₂Te₄ as a Cathode for a High Rate Performance Aqueous Zinc-Ion Battery

Li Wen, Yihua Gao, *et al.*

FEBRUARY 09, 2024

ACS NANO

READ ↗

Unraveling the Critical Role of Octahedrally Coordinated Mn in Spinel Manganites toward Enhanced Electrochemical Charge Storage

Yanli Gong, Peng Gao, *et al.*

SEPTEMBER 06, 2023

ACS SUSTAINABLE CHEMISTRY & ENGINEERING

READ ↗

Get More Suggestions >